


Cite this: *RSC Adv.*, 2022, 12, 29113

# First-principles study on the structural properties of 2D MXene SnSiGeN<sub>4</sub> and its electronic properties under the effects of strain and an external electric field†

Vo D. Dat,<sup>a</sup> Tuan V. Vu,<sup>a</sup> A. A. Lavrentyev,<sup>c</sup> O. Y. Khyzhun,<sup>d</sup> Nguyen N. Hieu<sup>\*ef</sup> and Hien D. Tong<sup>\*g</sup>

The MXene SnSiGeN<sub>4</sub> monolayer as a new member of the MoSi<sub>2</sub>N<sub>4</sub> family was proposed for the first time, and its structural and electronic properties were explored by applying first-principles calculations with both PBE and hybrid HSE06 approaches. The layered hexagonal honeycomb structure of SnSiGeN<sub>4</sub> was determined to be stable under dynamical effects or at room temperature of 300 K, with a rather high cohesive energy of 7.0 eV. The layered SnSiGeN<sub>4</sub> has a Young's modulus of 365.699 N m<sup>-1</sup> and a Poisson's ratio of 0.295. The HSE06 approach predicted an indirect band gap of around 2.4 eV for the layered SnSiGeN<sub>4</sub>. While the major donation from the N-p orbitals to the band structure makes SnSiGeN<sub>4</sub>'s band gap close to those of similar 2D MXenes, the smaller distributions from the other orbitals of Sn, Si, and Ge slightly vary this band gap. The work functions of the GeN and SiN surfaces are 6.367 eV and 5.903 eV, respectively. The band gap of the layered SnSiGeN<sub>4</sub> can be easily tuned by strain and an external electric field. A semiconductor–metal transition can occur at certain values of strain, and with an electric field higher than 5 V nm<sup>-1</sup>. The electron mobility of the layered SnSiGeN<sub>4</sub> can reach up to 677.4 cm<sup>2</sup> V<sup>-1</sup> s<sup>-1</sup>, which is much higher than the hole mobility of about 52 cm<sup>2</sup> V<sup>-1</sup> s<sup>-1</sup>. The mentioned characteristics make the layered SnSiGeN<sub>4</sub> a very promising material for use in electronic and photoelectronic devices, and for solar energy conversion.

Received 22nd August 2022  
Accepted 24th September 2022

DOI: 10.1039/d2ra05265b

rsc.li/rsc-advances

## 1 Introduction

After important achievements in the study and isolation of graphene, more and more 2D materials have become interesting subjects of scientific research, where the common target is to overcome modern problems, such as excessive energy consumption, environmental pollution, and the need for higher-efficiency electronic devices. The advantages of these 2D

materials come from their unique properties, including high charge-carrier mobility and thermal conductivity, tunable band gaps and electronic features, good mechanical characteristics, and the ability to be well-integrated in electronic devices.<sup>1–6</sup> Recently, the application of 2D materials has gone from theoretical prediction to practical uses. Monolayer graphene has been used in gamma and beta radiation sensors, and 2D Bi<sub>2</sub>Se<sub>3</sub> has been applied in photodetectors.<sup>7,8</sup> Both InSe and MoTe<sub>2</sub> have been shown to be very effective when used in field-effect transistors.<sup>9,10</sup> Moreover, hexagonal boron nitride has been applied in light-emitting diodes, and 2D WS<sub>2</sub> can improve the photocatalytic activity of mesoporous titania films.<sup>11</sup> Therefore, more and more 2D materials have been experimentally realized, including silicene, phosphorene, germanene, stanene, borophene, antimonene, arsenene, tellurene, selenene, bismuthene, aluminene, and gallene.<sup>12–22</sup>

In addition, transition metal chalcogenides (TMDs) are also very popular 2D materials consisting of transition metal elements and chalcogens. Monolayer TMDs are usually characterized as having strong spin–orbit coupling effects leading to a spin-valley phenomenon that, in combination with the buckled hexagonal structure, results in an enhancement of the quantum spin/anomalous Hall effects.<sup>23,24</sup> TMDs, depending on

<sup>a</sup>Laboratory for Computational Physics, Institute for Computational Science and Artificial Intelligence, Van Lang University, Ho Chi Minh City, Vietnam. E-mail: dat.vd@vlu.edu.vn

<sup>b</sup>Faculty of Mechanical – Electrical and Computer Engineering, Van Lang University, Ho Chi Minh City, Vietnam

<sup>c</sup>Department of Electrical Engineering and Electronics, Don State Technical University, 1 Gagarin Square, 344010 Rostov-on-Don, Russian Federation

<sup>d</sup>Frantsevych Institute for Problems of Materials Science, National Academy of Sciences of Ukraine, 3 Krzhizhanovsky Street, UA-03142 Kyiv, Ukraine

<sup>e</sup>Institute of Research and Development, Duy Tan University, Da Nang 550000, Vietnam. E-mail: hieunn@duytan.edu.vn

<sup>f</sup>Faculty of Natural Sciences, Duy Tan University, Da Nang 550000, Vietnam

<sup>g</sup>Faculty of Engineering, Vietnamese-German University, Binh Duong, Vietnam. E-mail: hien.td@vgu.edu.vn

† Electronic supplementary information (ESI) available. See <https://doi.org/10.1039/d2ra05265b>



their geometric structure and the d electrons of the transition metals, can be semiconducting, metallic, superconducting, and possess a charge density wave.<sup>25–35</sup> Janus 2D materials are a sub-branch of TMDs whose electronic properties are asymmetric, which may lead to strong Rashba spin splitting, piezoelectric polarization, and second-harmonic generation.<sup>36</sup>

MXenes are another branch of TMDs where one of the chalcogens is either an N or C element. Recently, 2D MoSiN<sub>4</sub> and WSiN<sub>4</sub> have been successfully synthesized and are considered to be another family of MXenes, whose structures are in the form of septuple-atomic-layers.<sup>37</sup> This study has inspired many other studies that predict the existence of many other compounds having the general formula MA<sub>2</sub>N<sub>4</sub>, where M represents transition metals W, V, Nb, Ta, Cr, Mo, Zr and Hf, and A represents chalcogens Si and Ge.<sup>38–40</sup> MXenes are very promising 2D materials as they have been shown to have great practical applications, including in electrode designs that allow new batteries to be charged much faster,<sup>41</sup> triboelectric nanogenerators,<sup>42</sup> conductive coatings with great flexibility,<sup>43</sup> and gas sensors.<sup>44</sup>

Theoretical studies predict that there are many more MXenes yet to be synthesized and with interesting properties to discover.<sup>45</sup> Therefore, the aim of the current study is to expand the family of MXenes with a septuple-atomic-layer structure by proposing and studying the properties of a SnSiGeN<sub>4</sub> monolayer. The mechanical and thermal stabilities of this material are justified based on the cohesive energy, phonon dispersion, elastic properties, including the Young's modulus and Poisson's ratio, and AIMD simulation. As mentioned above, MXenes can be applied in many devices where elasticity is sometimes highly required.<sup>46</sup> Meanwhile, it is well-known that the electronic properties of 2D materials can be greatly affected by strain and even an external electric field.<sup>47–51</sup> As a consequence, the effect of strain and an electric field on the properties of SnSiGeN<sub>4</sub> are also considered in this study.

## 2 Methodology

Based on the stable configurations of most compounds in the MoSi<sub>2</sub>N<sub>4</sub> family, the initial atomic structure of SnSiGeN<sub>4</sub> was simulated with space group *P3m1*, where the in-plane lattice parameters  $a = b = 3.083$  Å, and the normal lattice parameter  $c = 40$  Å, were used to prevent interaction between the atoms of neighboring unit cells. The Vienna Ab initio Simulation Package (VASP) was used to perform the structural optimization of SnSiGeN<sub>4</sub>, where the generalized gradient approximation parameterized by Perdew–Burke–Ernzerhof (PBE)<sup>52</sup> and the Heyd–Scuseria–Ernzerhof (HSE06)<sup>53</sup> hybrid functional were applied within the DFT framework. The buckling in the SnSiGeN<sub>4</sub> structure originates from the connection of the SnN<sub>2</sub>, SiN, and GeN planes. Therefore, the DFT-D3 (ref. 54) semi-empirical function was included in the calculation to account for the van der Waals interlayer interactions. The pseudopotentials used to describe the Sn, Si, Ge, and N atoms were generated by Kresse based on the projector-augmented wave (PAW) method<sup>55</sup> with an energy cut-off of 500 eV. The partial occupancies of the orbitals were described by the Gaussian smearing method with a smearing width of 0.05 eV. The

Monkhorst–Pack method was used to sample a  $16 \times 16 \times 1$  k-point mesh of the Brillouin zone. The structural optimization was converged when the difference in total energy of the atomic structure was smaller than  $10^{-4}$  eV, the force acting on the ions was about  $0.01$  eV Å<sup>-1</sup>, and the electron energy was 1 meV.

## 3 Results and discussion

### 3.1 Structural properties of the layered SnSiGeN<sub>4</sub>

The optimized structure of SnSiGeN<sub>4</sub>, shown in Fig. 1(a), is a layered structure whose *xy*-projection has a hexagonal shape with lattice parameters  $a = b = 3.083$  Å. This in-plane lattice parameter is very close to the values of 3.0282 Å and 3.143 Å of monolayers SnSi<sub>2</sub>N<sub>4</sub> and SnGe<sub>2</sub>N<sub>4</sub>, respectively,<sup>56,57</sup> and it is also comparable to those of MX<sub>2</sub>N<sub>4</sub> compounds (M = Hf, Zr, Ti, Cr, Mo, W, or Sn; X = Si or Ge), which range from 2.91 Å to 3.0282 Å.<sup>37,56,58,59</sup> The bond lengths  $d_2$  and  $d_3$  between Sn and the two nearest N atoms are about 2.18 Å, which is close to the range of 2.10–2.18 Å for the M–N bond lengths in MSiN<sub>4</sub> compounds (M = Mo, W, Cr, Ti, Zr, or Hf),<sup>60</sup> and it is also close to the Sn–N bond lengths of 2.166 Å and 2.2 Å in the two similar monolayers of SnSi<sub>2</sub>N<sub>4</sub> and SnGe<sub>2</sub>N<sub>4</sub>.<sup>56,57</sup> The side view of SnSiGeN<sub>4</sub> is depicted in Fig. 1(b), where the middle SnN<sub>2</sub> layer is stacked between the SiN and GeN layers *via* bonding with N atoms. The bond lengths between the N and Si atoms, and between the N and Ge atoms, are denoted as  $d_1$  and  $d_4$ , respectively. The Si–N, Ge–N, and Sn–N bond lengths are also very close to those in the SiN<sub>2</sub>, GeN<sub>2</sub>, and SnN<sub>2</sub> compounds that were obtained in previous theoretical and experimental studies.<sup>61,62</sup> As shown in Table 1, the bond lengths increase down group 14 from Si to Ge and Sn. This finding is consistent with an earlier experimental study on the pyrite forms of group 14 elements.<sup>62</sup> In comparison to Si<sub>3</sub>N<sub>4</sub>,<sup>63</sup> whose Si–N bond length is 1.89 Å, the bonding between Si and N atoms in SnSiGeN<sub>4</sub> is more covalent due to a shorter bond length of about 1.837 Å. The strength of the bonding in SnSiGeN<sub>4</sub> is also estimated by the cohesive energy  $E_{\text{coh}}$  of the layered SnSiGeN<sub>4</sub> in one unit cell by the following formula:

$$E_{\text{coh}} = \frac{(N_{\text{Sn}}E_{\text{Sn}} + N_{\text{Si}}E_{\text{Si}} + N_{\text{Ge}}E_{\text{Ge}} + N_{\text{N}}E_{\text{N}}) - E_{\text{tot}}}{N_{\text{Sn}} + N_{\text{Si}} + N_{\text{Ge}} + N_{\text{N}}} \quad (1)$$

where  $E_{\text{tot}}$  is the total energy of the monolayer SnSiGeN<sub>4</sub>, and  $E_{\text{Sn}}$ ,  $E_{\text{Si}}$ ,  $E_{\text{Ge}}$ , and  $E_{\text{N}}$  are the single-atom energies of Sn, Si, Ge, and N, respectively; and  $N_{\text{Sn}}$ ,  $N_{\text{Si}}$ ,  $N_{\text{Ge}}$ , and  $N_{\text{N}}$  stand for the number of Sn, Si, Ge and N atoms in the formula SnSiGeN<sub>4</sub>.

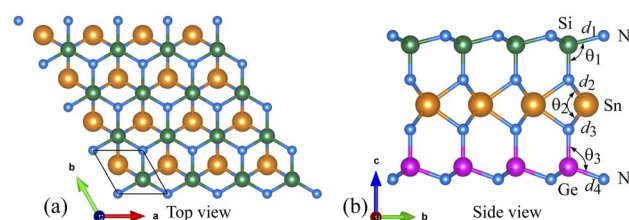


Fig. 1 (a) Top and (b) side views of the optimized SnSiGeN<sub>4</sub> in a layered structure.



**Table 1** The structural properties of SnSiGeN<sub>4</sub> including the in-plane lattice constant  $a$  (Å), N–Si bond length  $d_1$  (Å), first N–Sn bond length  $d_2$  (Å), second N–Sn bond length  $d_3$  (Å), N–Ge bond length  $d_4$  (Å), angle  $\theta_1$  between Si and the two nearest N atoms, angle  $\theta_2$  between Sn and the two nearest N atoms, angle  $\theta_3$  between Ge and the two nearest N atoms, and the cohesive energy  $E_{\text{coh}}$  (eV per atom)

$a$ (Å)	$d_1$ (Å)	$d_2$ (Å)	$d_3$ (Å)	$d_4$ (Å)	$\theta_1$ (deg)	$\theta_2$ (deg)	$\theta_3$ (deg)	$E_{\text{coh}}$ (eV per atom)
3.083	1.837	2.185	2.180	1.882	104.30	70.72	109.15	−7.004

The calculated cohesive energy of SnSiGeN<sub>4</sub> is −7.004 eV per atom. It is higher than those of phosphorene (−3.3 eV per atom), MoSi<sub>2</sub>P<sub>4</sub> (−5.5 eV per atom), and MoSi<sub>2</sub>As<sub>4</sub> (−6.1 eV per atom).<sup>64–66</sup> At the same time, this value is slightly smaller than those of graphene (−7.7 eV per atom) and MoSi<sub>2</sub>N<sub>4</sub> (−8.46 eV per atom).<sup>67,68</sup> As a result, the mechanical strength of the layered SnSiGeN<sub>4</sub> is predicted to be higher than that of phosphorene and some other members of the MoSi<sub>2</sub>N<sub>4</sub> family, but comparable to graphene and slightly lower than that of MoSi<sub>2</sub>N<sub>4</sub>. Furthermore, the mechanical stability of the layered SnSiGeN<sub>4</sub> can be estimated by its phonon dispersion, which was calculated and presented in Fig. 2(a).

As with other hexagonal structures, the highly symmetric path of the layered SnSiGeN<sub>4</sub> is  $\Gamma$ –M–K– $\Gamma$ , along which the phonon dispersion was calculated. All 21 vibrational modes originating from Sn, Si, Ge, and 4 N atoms are positive, confirming the layered SnSiGeN<sub>4</sub>'s dynamic stability. Because the acoustic branches have a low slope, the elastic modulus and

melting temperature of SnSiGeN<sub>4</sub> are expected to be moderate. It can also be seen in Fig. 2(a) that the gap between the optical and acoustic branches is very narrow, implying that heat transfer in the layered SnSiGeN<sub>4</sub> can be affected by optical effects. The thermal stability of the layered SnSiGeN<sub>4</sub> was also estimated by applying *ab initio* molecular dynamics (AIMD) to study the changes in total energy and temperature of this material when heated to 300 K for 6 ps. The total energy of the layered SnSiGeN<sub>4</sub> changes slightly in response to the extreme temperature fluctuation at the beginning of the heating process, as seen in Fig. 2(b and c). However, because the structure of the layered SnSiGeN<sub>4</sub> quickly returns to near-equilibrium states, both the total energy and temperature of the system fluctuate gradually. These findings support the thermal stability of the layered SnSiGeN<sub>4</sub>, as shown in Fig. 2(d), where the atomic structure of this semiconductor changes slightly during the heating process.

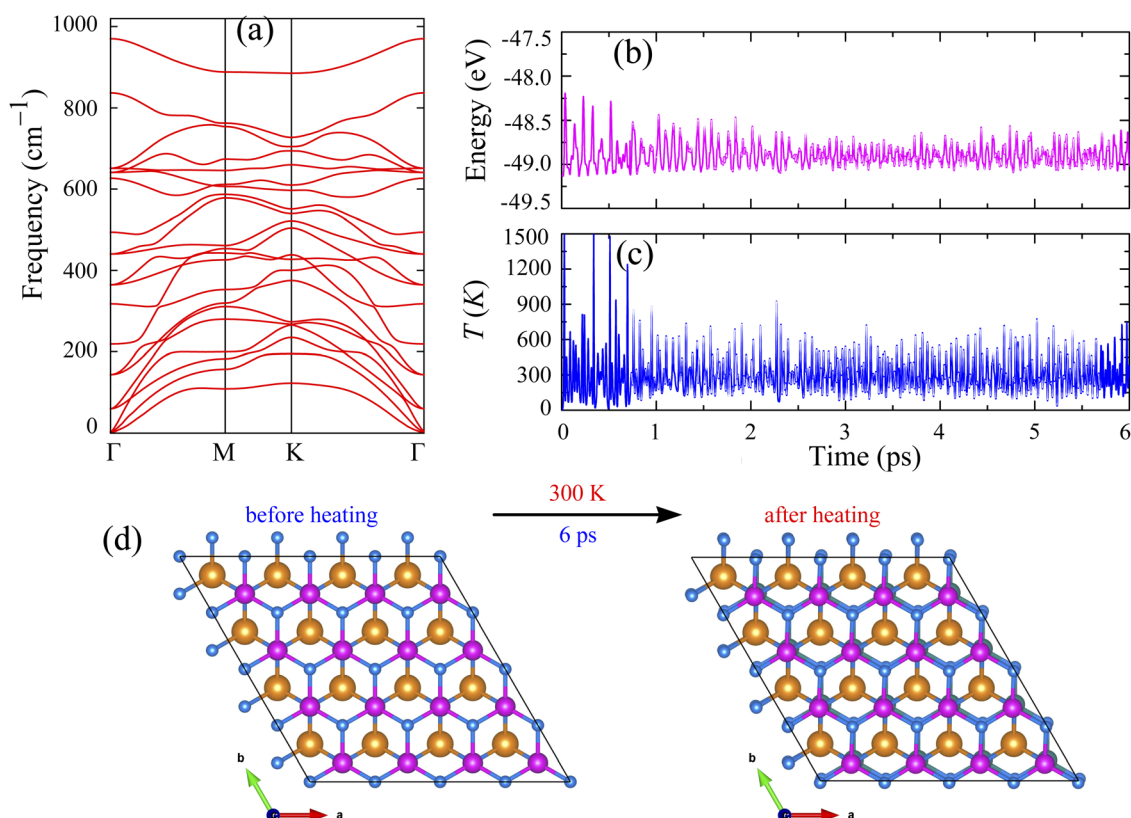


**Fig. 2** (a) Phonon dispersion of the layered SnSiGeN<sub>4</sub>, (b) total energy and (c) temperature of the layered SnSiGeN<sub>4</sub> as functions of time, and (d) top view of the layered SnSiGeN<sub>4</sub> before and after heating.



In the case of the SnSiGeN<sub>4</sub> monolayer, its mechanical stability can be investigated using Born–Huang's criteria<sup>69</sup> with elastic constants  $C_{ij}$ , shown in Table 2, where only  $C_{11}$  and  $C_{12}$  are required to be determined because  $C_{22} = C_{11}$ , and  $C_{66}$  is half the difference between  $C_{11}$  and  $C_{12}$ . These elastic constants can be calculated by fitting the values of elastic energy to different strains.<sup>70</sup> Both Born–Huang's criteria,  $C_{11} > 0$  and  $C_{11}^2 - C_{12}^2 > 0$ , are satisfied in the case of the SnSiGeN<sub>4</sub> monolayer, confirming the mechanical stability of this material.<sup>71</sup> Moreover, the Young's modulus  $Y_{2D}$  and Poisson's ratio  $\nu$  of the SnSiGeN<sub>4</sub> monolayer were also calculated as follows:

$$Y_{2D} = \frac{C_{11}^2 - C_{12}^2}{C_{11}}, \quad (2)$$

$$\nu = \frac{C_{12}}{C_{11}}. \quad (3)$$

The values of  $Y_{2D}$  and  $\nu$  are listed in Table 2. With a Young's modulus of 365.699 N m<sup>-1</sup>, the ability of the layered SnSiGeN<sub>4</sub> to withstand deformation under compression or tension is medium in comparison with other members of the MoSi<sub>2</sub>N<sub>4</sub> family, such as MoSi<sub>2</sub>As<sub>4</sub>, MoSi<sub>2</sub>P<sub>4</sub>, WSi<sub>2</sub>N<sub>4</sub>, and MoSi<sub>2</sub>N<sub>4</sub>, whose Young's modulus values are in the range of 118–600 N m<sup>-1</sup>.<sup>72,73</sup> The Poisson's ratio of 0.295 is generally considered to be low, therefore the layered SnSiGeN<sub>4</sub> is expected to be easily fractured. The Poisson's ratio of SnSiGeN<sub>4</sub> is very close to that of MoSiGeN<sub>4</sub> and WSiGeN<sub>4</sub> ( $\nu = 0.290$ – $0.296$ ) in the MoSi<sub>2</sub>N<sub>4</sub> family.<sup>58</sup> Generally, the SnSiGeN<sub>4</sub> monolayer is less mechanically stable than SnSi<sub>2</sub>N<sub>4</sub> and SnGe<sub>2</sub>N<sub>4</sub> due to its lower Young's

modulus and Poisson's ratio in comparison with these two similar compounds.<sup>56,57</sup> The existence of the SnSiGeN<sub>4</sub> monolayer can also be verified by comparing with experimental data, therefore, the theoretical X-ray diffraction pattern for SnSiGeN<sub>4</sub> was also calculated and is presented in Fig. S1 of the ESI.†

### 3.2 Electronic properties of the SnSiGeN<sub>4</sub> monolayer

Most members of the MoSi<sub>2</sub>N<sub>4</sub> family have been shown to be suitable for applications in optoelectronics and photocatalytic devices,<sup>38,73</sup> which usually require specific electronic structures. Therefore, it is interesting to study the electronic properties of the newly proposed SnSiGeN<sub>4</sub> compound. Since the layered SnSiGeN<sub>4</sub> has a symmetric hexagonal structure in the *x*–*y* plane, its band structure was calculated along the  $\Gamma$ –M–K– $\Gamma$  path. In Fig. 3(a), both the PBE and HSE06 methods reveal a direct band gap of the layered SnSiGeN<sub>4</sub> compound, where both the highest valence band and the lowest conduction band are located at the  $\Gamma$ -point. However, the band gaps of the SnSiGeN<sub>4</sub> monolayer reproduced by the two calculation methods differ by around 0.9 eV, with the PBE band gap being 1.446 eV and the HSE06 band gap being 2.396 eV. A similar difference in the band gaps calculated by the PBE and HSE06 methods is also found for SnSi<sub>2</sub>N<sub>4</sub> and SnGe<sub>2</sub>N<sub>4</sub> monolayers.<sup>56,57</sup> Furthermore, the HSE06 band gap of SnSiGeN<sub>4</sub> is located between those of SnSi<sub>2</sub>N<sub>4</sub> and SnGe<sub>2</sub>N<sub>4</sub>, which are 3.19 eV and 1.832 eV, respectively. Comparing the PBE band gap of the layered SnSiGeN<sub>4</sub> to those of its analogous 2D MXenes MoSiGeN<sub>4</sub> and WSiGeN<sub>4</sub>, which are 1.35 eV and 1.63 eV, respectively,<sup>58</sup> it is evident that the band gap changes moderately with the variation of Mo, W, and Sn metals. It is widely known that the poor handling of the exchange–correlation in PBE calculations leads to an underestimation of the band gap in semiconductors and insulators.<sup>74</sup> Therefore, the accuracy of the band gap can be increased by including a small portion of the accurate Hartree–Fock exchange in hybrid functionals, like HSE, B3LYP, and PBE0.<sup>75–77</sup> The band gap of the SnSiGeN<sub>4</sub> monolayer reproduced by the HSE06 method is 2.396 eV, which is in good agreement with the

**Table 2** Elastic constants  $C_{11}$ ,  $C_{12}$ , and  $C_{66}$  (N m<sup>-1</sup>), Young's modulus  $Y_{2D}$  (N m<sup>-1</sup>), and Poisson's ratio  $\nu$  of the layered SnSiGeN<sub>4</sub>

$C_{11}$	$C_{12}$	$C_{66}$	$Y_{2D}$	$\nu$
400.657	118.347	141.155	365.699	0.295

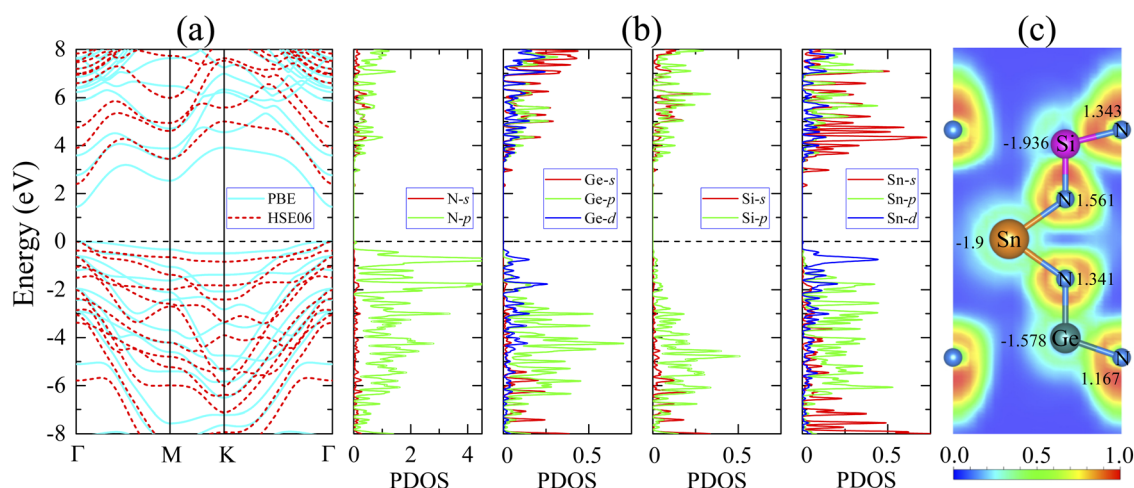


**Fig. 3** Electronic properties of the SnSiGeN<sub>4</sub> monolayer including (a) band structures obtained by the PBE method (blue solid lines) and the HSE06 method (red dashed lines), (b) partial density of states, (c) electron localization function and Bader charges.





PBE band gap values (2.396–2.70 eV)<sup>60,78</sup> of similar 2D compounds  $\text{MSi}_2\text{N}_4$  ( $\text{M} = \text{Mo}, \text{W}, \text{Ti}, \text{Zr}, \text{or Hf}$ ). The PBE and HSE06 band structures of the  $\text{SnSiGeN}_4$  monolayer (shown in Fig. 3(a) as blue solid lines and red dashed lines, respectively) were found to be comparable to one another. However, in the HSE06 calculations, the valence bands are moved to lower energy levels, while the conduction bands' energy levels are raised, resulting in widening of the band gap with HSE06. The four elements Sn, Si, Ge and N are close to one another in the  $\text{SnSiGeN}_4$  monolayer resulting in substantial orbital splitting, which is depicted in Fig. 3(b), with many peaks in both the valence and conduction bands. This advantage allows the  $\text{SnSiGeN}_4$  monolayer to absorb a wide range of solar wavelengths and be a promising material for solar energy conversion. The characteristics of the  $\text{SnSiGeN}_4$  monolayer band structure, Fig. 4, are well reflected by the weighted band structure. It can be seen that the band gap of  $\text{SnSiGeN}_4$  is largely established by the N-p orbitals, which contribute major portions to both the highest valence bands (HVBs) and the lowest conduction bands (LCBs), as in other 2D MXenes where the N element is the main component in the layered structures.<sup>58,60,78</sup> Meanwhile, the small deviation in the band gap of  $\text{SnSiGeN}_4$  from those of other 2D MXenes is caused by the minor contributions of the d orbitals of Sn and Ge atoms to the HVBs, as well as the s orbitals of Ge, Si, and Sn atoms to the LCBs. The bonding characteristics of the  $\text{SnSiGeN}_4$  monolayer are reflected by the electron localization function (ELF) in Fig. 3(c), where the regions with fully localized electrons, fully delocalized electrons, and extremely low electron density are denoted by red (1.0), green (0.5), and blue (0.0) colors, respectively. Most localized electrons are observed to concentrate around the N atoms, whereas the regions between all atoms are fully occupied by delocalized electrons, demonstrating the covalent nature of the bonding in the  $\text{SnSiGeN}_4$  monolayer.

Many 2D MXenes similar to  $\text{SnSiGeN}_4$  have been discovered to be promising materials for photoelectric applications,<sup>57,79</sup> where the work function plays one of the most important roles.<sup>80–82</sup> Therefore, modification of the work function of 2D materials has long been an interesting research subject.<sup>83</sup> The work functions of the  $\text{SnSiGeN}_4$  monolayer were calculated by eqn (4), as shown below, and are shown in Fig. 5 as  $\Phi_1$  (6.367 eV)

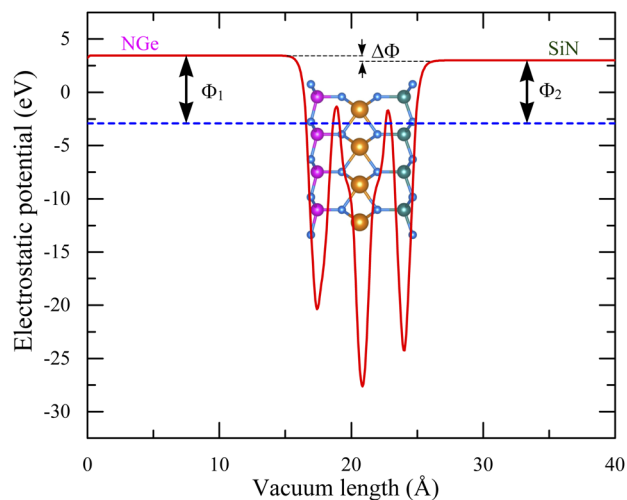


Fig. 5 Work functions of the  $\text{SnSiGeN}_4$  monolayer.

and  $\Phi_2$  (5.903 eV) for the NGe and NSi surfaces, respectively. These work functions are comparable to those of a  $\text{MoGe}_2\text{N}_4$  monolayer (5.44 eV) and  $\text{SnSi}_2\text{N}_4$  (6.20 eV).<sup>56,84</sup> It is interesting to note that the work function of  $\text{SnGe}_2\text{N}_4$  (6.216 eV)<sup>57</sup> is a little bit higher than that of  $\text{SnSi}_2\text{N}_4$  (6.20 eV).<sup>56</sup> Meanwhile, the work function of the  $\text{SnSi}_2\text{N}_4$  surface can be enhanced by about 0.2 eV by substituting one Si by one Ge atom to form a  $\text{SnSiGeN}_4$  monolayer. Because  $p_z$  orbitals are important in determining the magnitude of the work function in 2D materials,<sup>85</sup> the occupation of Ge-p and Sn-p orbitals at different energy levels in the HVBs, as seen in Fig. 4, is expected to account for a potential drop of around  $\Delta\Phi = 0.464$  eV. This anisotropy is favorable for the separation of photo-driven electron-hole pairs. Another advantage of the  $\text{SnSiGeN}_4$  monolayer is that its work function values are in the range of 4–7 eV, which have been shown to be suitable for optoelectronics and photoelectric applications.<sup>86,87</sup>

$$\Phi = \Phi_{\text{vac}} - \Phi_{\text{F}} \quad (4)$$

where  $\Phi_{\text{vac}}$  is the electrostatic potential in the vacuum near the surface, and  $\Phi_{\text{F}}$  is the electrochemical potential per electron at the Fermi level inside the material.

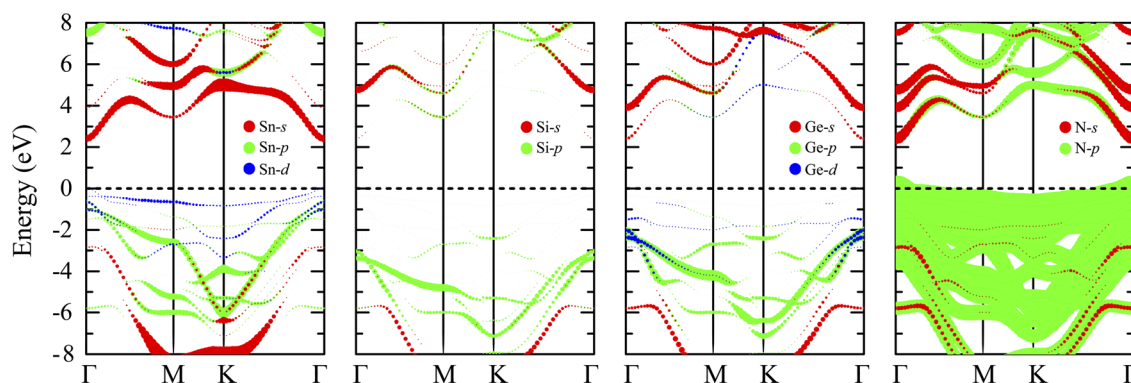


Fig. 4 Weighted band structure of the  $\text{SnSiGeN}_4$  monolayer with the HSE06 method.



The band structure of most 2D materials can be easily tuned by strain<sup>88,89</sup> because the decrease of symmetry can greatly affect the Hamiltonian function.<sup>90</sup> Moreover, an external electric field has also been reported to influence the band structure of some special semiconductors, such as phosphorene/graphene-like GaN, a SnS<sub>2</sub>/PbI<sub>2</sub> heterostructure, and two-dimensional transition metal dichalcogenides.<sup>91–93</sup> 2D materials whose band gap is tunable play an important role in electrical and optoelectronic devices.<sup>93</sup> In order to investigate the potential of the SnSiGeN<sub>4</sub> monolayer for application in the mentioned areas, its band structure under the effect of strains ranging from –10% to 10%, and an electric field whose magnitude is –5 V nm<sup>–1</sup> to 5 V nm<sup>–1</sup> is explored. The primary effect of compressive strains on the band structure is a redistribution in the band edges. As illustrated in Fig. 6(a and b), the higher the strain rate, the more the valence bands are concave up and the conduction bands are concave down, indicating that the mobility of electrons and holes would rise. Tensile strains, on the other hand, tend to flatten the valence and conduction bands, therefore, these strains are expected to reduce the charge-carrier mobility in the layered SnSiGeN<sub>4</sub>. Compressive and tensile strains have a considerable influence on the energy levels of the band edges, with some minor redistribution of the extrema of the valence and conduction bands. As a result, the nature and amplitude of the band gap in the layered SnSiGeN<sub>4</sub> are likely to be modified. To further comprehend this problem, the change in band gap of

the layered SnSiGeN<sub>4</sub> as a discrete function of strain is shown in Fig. 6(c). The band gap increases to its maximum value of about 2 eV at –6% compression. As the compressive strain increases, the band gap decreases significantly, and the direct band gap transforms into an indirect band gap. All tensile strains generate a fast reduction in the band gap, during which the indirect band gap becomes direct at roughly 1% tensile strain and returns to being indirect at greater tensile rates. The electronic structure of the SnSiGeN<sub>4</sub> monolayer changes in a similar way to the SnGe<sub>2</sub>N<sub>4</sub> monolayer, where compressive strains tend to enlarge the band gap and tensile strains cause the band gap to narrow.<sup>57</sup> External electric fields have a negligible effect on the form of the valence and conduction bands, as seen in Fig. 6(d and e), while the band gap remains constant. An external electric field with a magnitude of 4 V nm<sup>–1</sup> was discovered to be the critical point affecting SnSiGeN<sub>4</sub>'s band structure, as illustrated in Fig. 6(f), where the band gap begins to decrease dramatically. The layered SnSiGeN<sub>4</sub> was also observed to turn into a metal under a tensile strain of 10%, as shown in Fig. 6(c). However, this is a theoretical prediction where the stability of the SnSiGeN<sub>4</sub> structure under very high strains must be carefully verified. Actually, there are many 2D structures that have been proven, both experimentally and theoretically, to be stable at strains higher than 6–10%,<sup>94</sup> therefore, this phenomenon of the layered SnSiGeN<sub>4</sub> is an interesting subject for further studies.

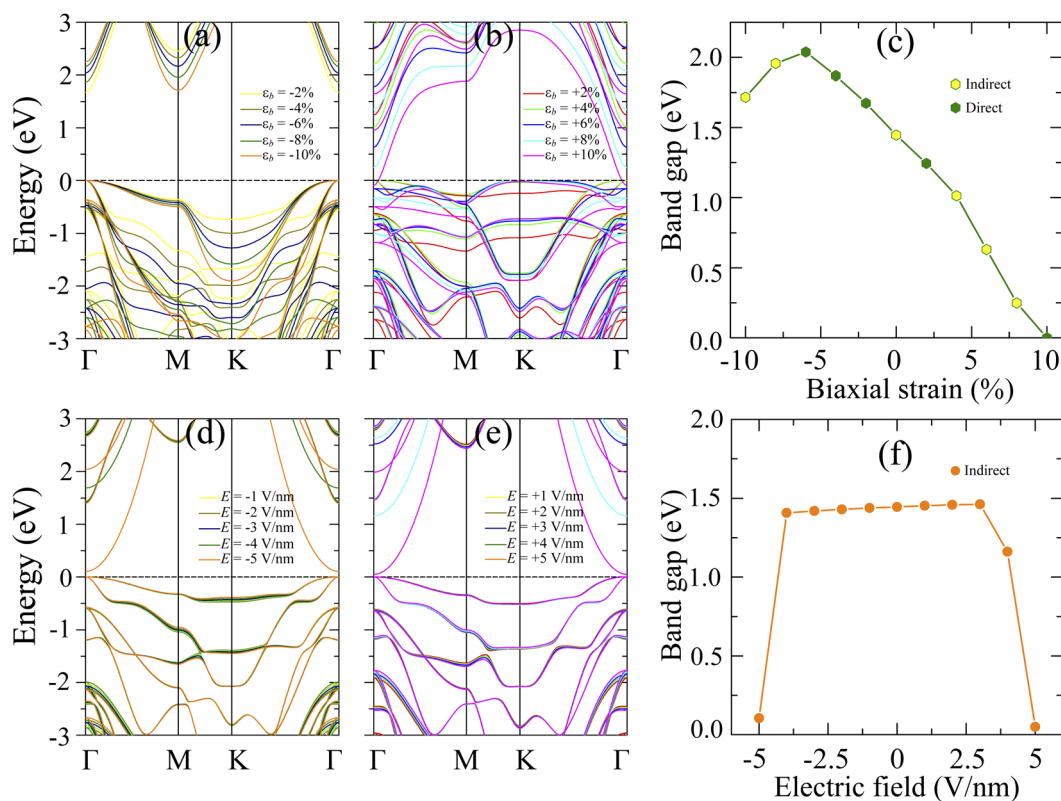


Fig. 6 Band structures of the SnSiGeN<sub>4</sub> monolayer under the effect of (a) compressive strain, (b) tensile strain, (d) an external negative electric field and (e) an external positive electric field. (c) The band gap as a function of biaxial strain and (f) the band gap as a function of an external electric field.



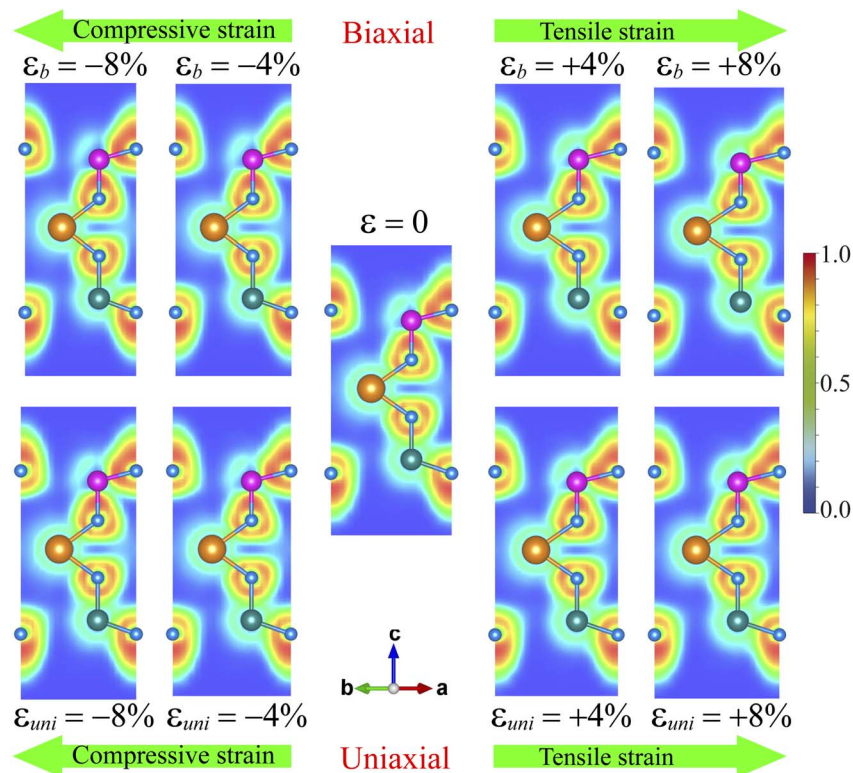


Fig. 7 Electron localization function of SnSiGeN<sub>4</sub> under biaxial/uniaxial compressive strains, at equilibrium, and under biaxial/uniaxial tensile strains.

The variation of SnSiGeN<sub>4</sub>'s band structure under strain, as shown in Fig. 8, is very interesting and it can cause a change in the mobility of the charge carrier. In order to uncover the mechanism causing these effects and how it can affect the transport properties of the SnSiGeN<sub>4</sub> monolayer, it is necessary to analyze the redistribution of electrons in the structures under some representative strain rates of 4% and 8%. Therefore, the electron localization function and Bader charges were calculated for both biaxial and uniaxial strains. The ELF shown in Fig. 7 and the Bader charges (see Tables S1 and S2 of the ESI†) of the compressively strained, unstrained, and tensile-strained SnSiGeN<sub>4</sub> monolayer are depicted from left to right. Similar to Fig. 3(c), the green area represents fully delocalized electrons, the red regions correspond to fully localized electrons and the regions with low electron density are blue. The changes in the band gap of SnSiGeN<sub>4</sub> as a function of biaxial and uniaxial strains are presented in Fig. S2 of the ESI.†

Both biaxial and uniaxial strains cause similar effects. Under increasing compressive strain, the green regions spread out more between the atoms, indicating a higher level of covalent bonding. Meanwhile, the tensile strains cause wider spaces between the green regions, reflecting a decrease in the overlap between the valence electrons of neighboring atoms in the SnSiGeN<sub>4</sub> monolayer. The Bader charge data show that, under compressive strains, more electrons are transferred from the metals to the N atoms. Consequently, the partly empty 2p orbital of N receives more electrons, lowering the conduction bands at the M-point in Fig. 4. At the same time, the Sn atoms

lose their electrons from the 5s<sup>2</sup> and 5p<sup>2</sup> orbitals; this raises the conduction bands at the  $\Gamma$ -points. Considering Fig. 3, it is obvious that the Sn-s orbitals mainly donate to the lowest conduction bands, and the N-p orbitals dominate the highest valence bands. As long as the conduction bands at the  $\Gamma$ -point are higher than those at the M-point, the band gap of SnSiGeN<sub>4</sub> still widens under compressive strains. When the conduction bands at the M-point are lower than those at the  $\Gamma$ -points, SnSiGeN<sub>4</sub> has an indirect band gap, which is also narrowed. Under tensile strains, charge transfer happens in the reverse direction when more electrons stay in the 5s<sup>2</sup> and 5p<sup>2</sup> orbitals of the Sn atoms, causing a narrower gap between the valence and conduction bands at the  $\Gamma$ -points, which leads to the decreasing of the SnSiGeN<sub>4</sub>'s band gap at low tensile rates. At higher tensile rates, the valence and conduction bands at the  $\Gamma$ -point overlap each other, making the SnSiGeN<sub>4</sub> monolayer a metal. The highest valence band also fluctuates strongly due to fewer electrons being concentrated on the N atoms.

Generally, both compressive and tensile strains cause the redistribution of charge density, which can be observed from the ELF and Bader charge plots. This change affects the occupation of electrons in the valence bands (mainly constructed by N-p orbitals) and conduction bands (largely donated to by Sn-s orbitals) causing some fluctuations in the extrema of these bands. As a result, the band gap is tuned. Because the effective mass is proportional to the derivative of the band-edge curves, a change in the shape of the conduction and valence band edges can cause a change in the mobility of electrons and holes. As



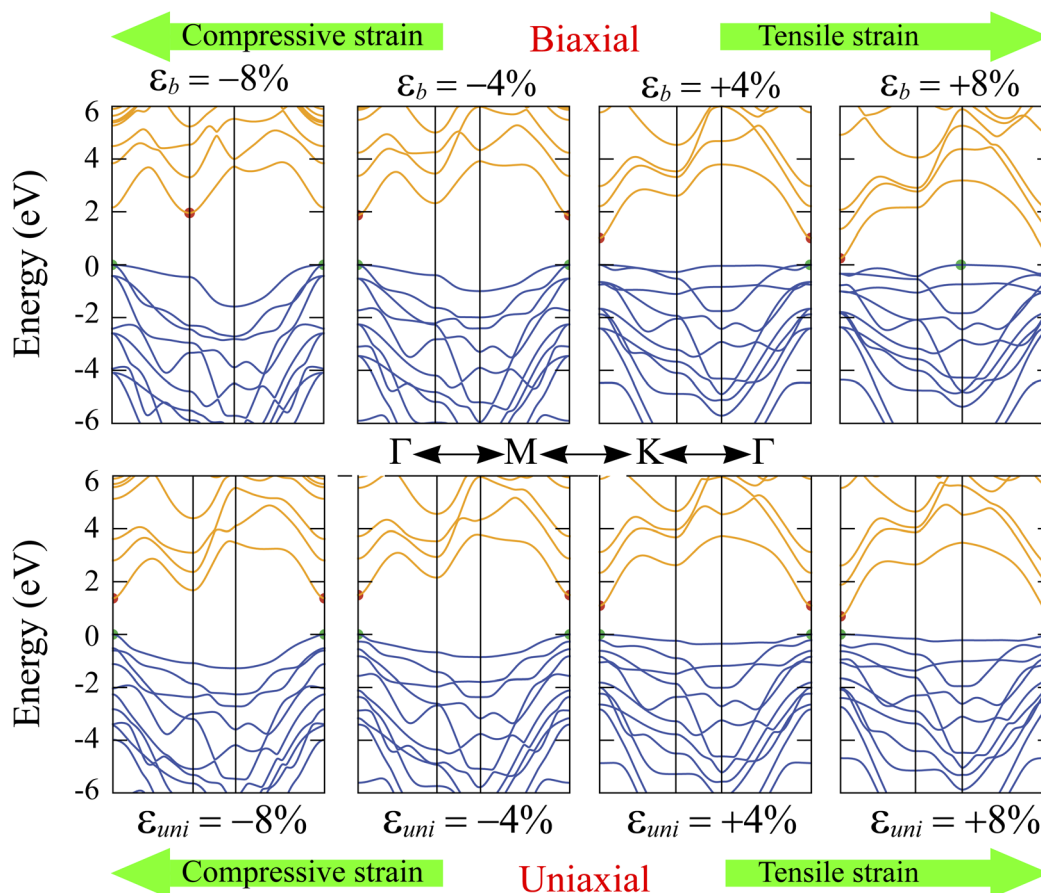


Fig. 8 Band structure of SnSiGeN<sub>4</sub> under biaxial and uniaxial strains.

shown in Fig. 8, the tensile strains tend to flatten the valence bands, therefore, it is expected that the effective mass of the hole is decreased. Meanwhile, the hole's effective mass may increase as the valence bands are more concave down under compressive strains. Analogously, the effective mass of the electron is expected to be higher as the peaks in the lowest conduction bands are sharper under strain.

### 3.3 Transport properties of the SnSiGeN<sub>4</sub> monolayer

The charge-carrier mobility  $\mu_{2D}$  for the layered SnSiGeN<sub>4</sub> was calculated based on deformation potential theory.<sup>95</sup> Firstly, the total energy  $E$ , and band-edge alignment  $\Delta E_{\text{edge}}$  were calculated and constructed as functions of uniaxial strain  $\epsilon_{\text{uni}}$  along the  $x$ -axis and  $y$ -axis. The  $E(\epsilon_u)$  and  $\Delta E_{\text{edge}}(\epsilon_{\text{uni}})$  functions are

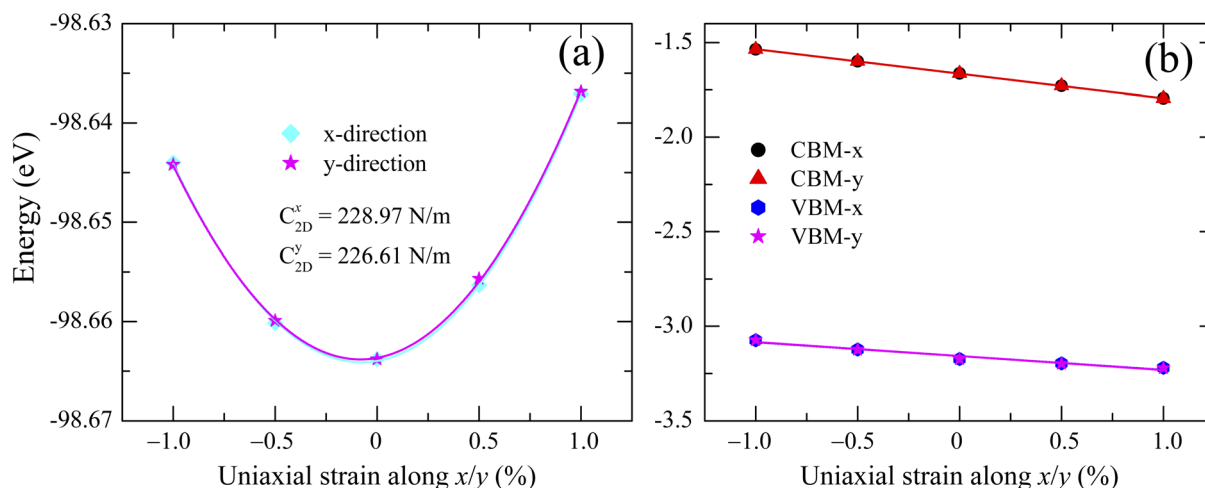


Fig. 9 (a) Strain-dependent total energy and (b) the band-edge positions of the SnSiGeN<sub>4</sub> structures along the two transport directions  $x$  and  $y$ .





presented in Fig. 9(a and b), respectively. Moreover, the dependence of total energy  $E(k)$  on the  $k$ -points was also constructed. Then, the effective mass  $m^*$ , the elastic modulus  $C_{2D}$ , and the deformation energy constant  $E_d$ , were as follows:

$$\frac{1}{m^*} = \frac{1}{\hbar^2} \left| \frac{\partial^2 E(k)}{\partial k^2} \right|, \quad (5)$$

$$C_{2D} = \frac{1}{\Omega_0} \frac{\partial^2 E}{\partial \varepsilon_{\text{uni}}^2}, \quad (6)$$

$$E_d = \frac{\Delta E_{\text{edge}}}{\varepsilon_{\text{uni}}}, \quad (7)$$

where the letters  $\hbar$  and  $\Omega_0$  stand for the reduced Planck constant and the volume of the unit cell, respectively.

Finally, the charge-carrier mobility  $\mu_{2D}$  was calculated as follows:

$$\mu_{2D} = \frac{e\hbar^3 C_{2D}}{k_B T m^* \bar{m} E_d^2}, \quad (8)$$

where the letters  $e$  and  $k_B$  stand for the elementary charge of an electron and the Boltzmann constant, respectively.

The layered SnSiGeN<sub>4</sub> has a symmetric hexagonal structure in the  $x$ - $y$  plane, therefore, its charge-carrier mobilities and related quantities, as shown in Table 3, are independent of the direction along which they were determined. They are, however, dependent on the energy functions of the  $k$ -point, as given in eqn (5)–(7). The effective masses are inversely proportional to the second derivatives of the energy functions, according to eqn (5). As a result, the layered SnSiGeN<sub>4</sub> with sharply curved conduction bands and relatively flat valence bands, as shown in Fig. 4, has a lower electron effective mass than hole effective mass. These characteristics cause the electron mobility to be greater than the hole mobility, which are 670.83–677.4 cm<sup>2</sup> V<sup>−1</sup> s<sup>−1</sup> and 50.2–51.9 cm<sup>2</sup> V<sup>−1</sup> s<sup>−1</sup>, respectively. Considering the charge-carrier mobilities of SnSi<sub>2</sub>N<sub>4</sub> and SnGe<sub>2</sub>N<sub>4</sub> (electron mobilities of 2735.97 and 1061.66 cm<sup>2</sup> V<sup>−1</sup> s<sup>−1</sup>, respectively),<sup>56,57</sup> it is obvious that the substitution of one Si atom in SnSi<sub>2</sub>N<sub>4</sub> by one Ge atom to form SnSiGeN<sub>4</sub> causes a significant decrease of the electron mobility. The layered SnSiGeN<sub>4</sub> has greater electron mobility than other similar 2D compounds, MX<sub>2</sub>N<sub>4</sub> (M = Mo or W; X = Ge or Si).<sup>38</sup> It's worth noticing that the post-transition metal Sn produces an opposite charge-carrier mobility pattern compared to other compounds in the MoSi<sub>2</sub>N<sub>4</sub> family, MX<sub>2</sub>Y<sub>4</sub> (M = V, Cr, Mo, or W; X = Si or C; Y = N, P, or As),<sup>66,96</sup> where the electron mobility is substantially lower than the hole mobility. A similar phenomenon has been reported in monolayers of SnGe<sub>2</sub>N<sub>4</sub> and SnSi<sub>2</sub>N<sub>4</sub>.<sup>56,57</sup>

**Table 3** Effective mass  $m^*$  of electron and hole ( $m_0$ ), elastic modulus  $C_{2D}$  (N m<sup>−1</sup>), deformation potential constant  $E_d$  (eV), and carrier mobility  $\mu$  (cm<sup>2</sup> V<sup>−1</sup> s<sup>−1</sup>) along the  $x/y$ -direction of SnSiGeN<sub>4</sub> single layers.  $m_0$  is the free electron mass

	$m_x^*$	$m_y^*$	$C_{2D}^x$	$C_{2D}^y$	$E_d^x$	$E_d^y$	$\mu_x$	$\mu_y$
Electron	0.21	0.21	228.97	226.61	−12.97	−12.96	677.4	670.83
Hole	−1	−1	228.97	226.61	−7.33	−7.42	51.92	50.2

## 4 Conclusions

In conclusion, the atomic, electronic, and transport characteristics of a SnSiGeN<sub>4</sub> monolayer were investigated by first-principles calculations. The theoretical results show that the SnSiGeN<sub>4</sub> monolayer is dynamically, mechanically, and thermally stable. The band gap of the layered SnSiGeN<sub>4</sub> was estimated to be about 2.4 eV, which is easily tuned by strain. Both strain and an external electric field at some specific values can cause the SnSiGeN<sub>4</sub> monolayer to change from a semiconductor to a metal. Being an indirect semiconductor with a suitable band gap to absorb visible light and a high electron mobility of 677.4 cm<sup>2</sup> V<sup>−1</sup> s<sup>−1</sup>, SnSiGeN<sub>4</sub> monolayers are very promising materials for application in nanoelectronics.

## Conflicts of interest

There are no conflicts to declare.

## Acknowledgements

The authors gratefully appreciate the useful discussion of O. V. Marchuk (Department of Chemistry and Technology, Lesya Ukrainka Volyn National University, Lutsk, Ukraine).

## References

- M. C. Lemme, D. Akinwande, C. Huyghebaert and C. Stampfer, *Nat. Commun.*, 2022, **13**, 1392.
- E. Singh, P. Singh, K. S. Kim, G. Y. Yeom and H. S. Nalwa, *ACS Appl. Mater. Interfaces*, 2019, **11**, 11061–11105.
- S. Yang, C. Jiang and S.-h. Wei, *Appl. Phys. Rev.*, 2017, **4**, 021304.
- X. Wang, S. Kajiyama, H. Iinuma, E. Hosono, S. Oro, I. Moriguchi, M. Okubo and A. Yamada, *Nat. Commun.*, 2015, **6**, 6544.
- X. Xi, Z. Wang, W. Zhao, J.-H. Park, K. T. Law, H. Berger, L. Forró, J. Shan and K. F. Mak, *Nat. Phys.*, 2016, **12**, 139–143.
- Q. H. Wang, K. Kalantar-Zadeh, A. Kis, J. N. Coleman and M. S. Strano, *Nat. Nanotechnol.*, 2012, **7**, 699–712.
- M. W. Tawfik, A. Sharaf and M. Serry, *Nanomaterials*, 2022, **12**, 305.
- C.-C. Wang, P.-T. Lin, F.-S. Shieu and H.-C. Shih, *Nanomaterials*, 2021, **11**, 3353.
- Y. Zhang, X. Sun, K. Jia, H. Yin, K. Luo, J. Yu and Z. Wu, *Nanomaterials*, 2021, **11**, 3311.
- G. Y. Bae, J. Kim, J. Kim, S. Lee and E. Lee, *Nanomaterials*, 2021, **11**, 2805.
- J. Ren, L. Stagi, L. Malfatti, V. Paolucci, C. Cantalini, S. Garroni, M. Mureddu and P. Innocenzi, *Nanomaterials*, 2022, **12**, 1074.
- B. Aufray, A. Kara, S. Vizzini, H. Oughaddou, C. Léandri, B. Ealet and G. Le Lay, *Appl. Phys. Lett.*, 2010, **96**, 183102.
- W. Li, M. Li, J. Li, J. Liang, K. R. Adair, Y. Hu, Q. Xiao, X. Cui, R. Li, F. Brandys, et al., *ACS Appl. Nano Mater.*, 2020, **3**, 7508–7515.



- 14 E. Bianco, S. Butler, S. Jiang, O. D. Restrepo, W. Windl and J. E. Goldberger, *ACS Nano*, 2013, **7**, 4414–4421.
- 15 J. Ouyang, L. Zhang, L. Li, W. Chen, Z. Tang, X. Ji, C. Feng, N. Tao, N. Kong, T. Chen, et al., *Nano-Micro Lett.*, 2021, **13**, 90.
- 16 V. Kochat, A. Samanta, Y. Zhang, S. Bhowmick, P. Manimunda, S. A. S. Asif, A. S. Stender, R. Vajtai, A. K. Singh, C. S. Tiwary, et al., *Sci. Adv.*, 2018, **4**, e1701373.
- 17 M. O. Valappil, A. Ganguly, J. Benson, V. K. Pillai, S. Alwarappan and P. Papakonstantinou, *RSC Adv.*, 2020, **10**, 43585–43591.
- 18 C. Gibaja, M. Assebban, I. Torres, M. Fickert, R. Sanchis-Gual, I. Brotons, W. S. Paz, J. J. Palacios, E. G. Michel, G. Abellán, et al., *J. Mater. Chem. A*, 2019, **7**, 22475–22486.
- 19 S. Chahal, P. Ranjan, M. Motlag, S. S. Yamijala, D. J. Late, E. H. S. Sadki, G. J. Cheng and P. Kumar, *Adv. Mater.*, 2021, **33**, 2102039.
- 20 Z. Xie, C. Xing, W. Huang, T. Fan, Z. Li, J. Zhao, Y. Xiang, Z. Guo, J. Li, Z. Yang, et al., *Adv. Funct. Mater.*, 2018, **28**, 1705833.
- 21 S. M. Beladi-Mousavi, A. M. Pourrahimi, Z. Sofer and M. Pumera, *Adv. Funct. Mater.*, 2019, **29**, 1807004.
- 22 P.-Y. Liao, J.-K. Qin, G. Qiu, Y. Wang, W. Wu and D. Y. Peide, *Xenes*, Elsevier, 2022, pp. 197–224.
- 23 C. Liu, Y. Wang, H. Li, Y. Wu, Y. Li, J. Li, K. He, Y. Xu, J. Zhang and Y. Wang, *Nat. Mater.*, 2020, **19**, 522–527.
- 24 G.-B. Liu, W.-Y. Shan, Y. Yao, W. Yao and D. Xiao, *Phys. Rev. B: Condens. Matter Mater. Phys.*, 2013, **88**, 085433.
- 25 M. Chhowalla, H. S. Shin, G. Eda, L.-J. Li, K. P. Loh and H. Zhang, *Nat. Chem.*, 2013, **5**, 263–275.
- 26 G. Eda, H. Yamaguchi, D. Voiry, T. Fujita, M. Chen and M. Chhowalla, *Nano Lett.*, 2011, **11**, 5111–5116.
- 27 Y. Venkata Subbaiah, K. Saji and A. Tiwari, *Adv. Funct. Mater.*, 2016, **26**, 2046–2069.
- 28 K. F. Mak, C. Lee, J. Hone, J. Shan and T. F. Heinz, *Phys. Rev. Lett.*, 2010, **105**, 136805.
- 29 A. A. Soluyanov, D. Gresch, Z. Wang, Q. Wu, M. Troyer, X. Dai and B. A. Bernevig, *Nature*, 2015, **527**, 495–498.
- 30 D. H. Keum, S. Cho, J. H. Kim, D.-H. Choe, H.-J. Sung, M. Kan, H. Kang, J.-Y. Hwang, S. W. Kim, H. Yang, et al., *Nat. Phys.*, 2015, **11**, 482–486.
- 31 N. E. Staley, J. Wu, P. Eklund, Y. Liu, L. Li and Z. Xu, *Phys. Rev. B: Condens. Matter Mater. Phys.*, 2009, **80**, 184505.
- 32 A. F. Kusmartseva, B. Sipos, H. Berger, L. Forro and E. Tutiš, *Phys. Rev. Lett.*, 2009, **103**, 236401.
- 33 B. Sipos, A. F. Kusmartseva, A. Akrap, H. Berger, L. Forró and E. Tutiš, *Nat. Mater.*, 2008, **7**, 960–965.
- 34 T. Kidd, T. Miller, M. Chou and T.-C. Chiang, *Phys. Rev. Lett.*, 2002, **88**, 226402.
- 35 G. Li, W. Hu, D. Qian, D. Hsieh, M. Hasan, E. Morosan, R. J. Cava and N. Wang, *Phys. Rev. Lett.*, 2007, **99**, 027404.
- 36 L. Zhang, Z. Yang, T. Gong, R. Pan, H. Wang, Z. Guo, H. Zhang and X. Fu, *J. Mater. Chem. A*, 2020, **8**, 8813–8830.
- 37 Y.-L. Hong, Z. Liu, L. Wang, T. Zhou, W. Ma, C. Xu, S. Feng, L. Chen, M.-L. Chen, D.-M. Sun, et al., *Science*, 2020, **369**, 670–674.
- 38 B. Mortazavi, B. Javvaji, F. Shojaei, T. Rabczuk, A. V. Shapeev and X. Zhuang, *Nano Energy*, 2021, **82**, 105716.
- 39 A. Priyadarshi, Y. S. Chauhan, S. Bhowmick and A. Agarwal, *Nanoscale*, 2022, **14**, 11988–11997.
- 40 Y. Chen, S. Tian and Q. Tang, *J. Phys. Chem. C*, 2021, **125**, 22581–22590.
- 41 M. R. Lukatskaya, S. Kota, Z. Lin, M.-Q. Zhao, N. Shpigel, M. D. Levi, J. Halim, P.-L. Taberna, M. W. Barsoum, P. Simon, et al., *Nat. Energy*, 2017, **2**, 17105.
- 42 Y. Dong, S. S. K. Mallineni, K. Maleski, H. Behlow, V. N. Mochalin, A. M. Rao, Y. Gogotsi and R. Podila, *Nano Energy*, 2018, **44**, 103–110.
- 43 H. An, T. Habib, S. Shah, H. Gao, M. Radovic, M. J. Green and J. L. Lutkenhaus, *Sci. Adv.*, 2018, **4**, eaaq0118.
- 44 S. J. Kim, H.-J. Koh, C. E. Ren, O. Kwon, K. Maleski, S.-Y. Cho, B. Anasori, C.-K. Kim, Y.-K. Choi, J. Kim, et al., *ACS Nano*, 2018, **12**, 986–993.
- 45 T. L. Tan, H. M. Jin, M. B. Sullivan, B. Anasori and Y. Gogotsi, *ACS Nano*, 2017, **11**, 4407–4418.
- 46 W. Lu, B. Mustafa, Z. Wang, F. Lian and G. Yu, *Nanomaterials*, 2022, **12**, 871.
- 47 G. J. Kraberger, D. A. Egger and E. Zofer, *Adv. Mater. Interfaces*, 2015, **2**, 1500323.
- 48 G. G. Naumis, S. Barraza-Lopez, M. Oliva-Leyva and H. Terrones, *Rep. Prog. Phys.*, 2017, **80**, 096501.
- 49 H. Jiang, L. Zheng, Z. Liu and X. Wang, *InfoMat*, 2020, **2**, 1077–1094.
- 50 M. A. Bissett, M. Tsuji and H. Ago, *Phys. Chem. Chem. Phys.*, 2014, **16**, 11124–11138.
- 51 W. Chen, X. Gui, L. Yang, H. Zhu and Z. Tang, *Nanoscale Horiz.*, 2019, **4**, 291–320.
- 52 J. P. Perdew, K. Burke and M. Ernzerhof, *Phys. Rev. Lett.*, 1996, **77**, 3865–3868.
- 53 J. Heyd, G. E. Scuseria and M. Ernzerhof, *J. Chem. Phys.*, 2003, **118**, 8207–8215.
- 54 S. Grimme, J. Antony, S. Ehrlich and H. Krieg, *J. Chem. Phys.*, 2010, **132**, 154104.
- 55 G. Kresse and D. Joubert, *Phys. Rev. B: Condens. Matter Mater. Phys.*, 1999, **59**, 1758.
- 56 M. Tian, C. Wei, J. Zhang, J. Wang and R. Yang, *Phys. Rev. B: Condens. Matter Mater. Phys.*, 2021, **103**, 195305.
- 57 V. D. Dat and T. V. Vu, *RSC Adv.*, 2022, **12**, 10249–10257.
- 58 S.-D. Guo, W.-Q. Mu, Y.-T. Zhu, R.-Y. Han and W.-C. Ren, *J. Mater. Chem. C*, 2021, **9**, 2464–2473.
- 59 S.-D. Guo, Y.-T. Zhu, W.-Q. Mu and W.-C. Ren, *Europhys. Lett.*, 2020, **132**, 57002.
- 60 Y. Yin, M. Yi and W. Guo, *ACS Appl. Mater. Interfaces*, 2021, **13**, 45907–45915.
- 61 R. Wehrich, V. Eyert and S. F. Matar, *Chem. Phys. Lett.*, 2003, **373**, 636–641.
- 62 K. Niwa, H. Ogasawara and M. Hasegawa, *Dalton Trans.*, 2017, **46**, 9750–9754.
- 63 B. Xu, J. Dong, P. F. McMillan, O. Shebanova and A. Salamat, *Phys. Rev. B: Condens. Matter Mater. Phys.*, 2011, **84**, 014113.
- 64 J. Guan, Z. Zhu and D. Tománek, *Phys. Rev. Lett.*, 2014, **113**, 226801.
- 65 P.-J. Chen and H.-T. Jeng, *Sci. Rep.*, 2016, **6**, 23151.



- 66 H. Yao, C. Zhang, Q. Wang, J. Li, Y. Yu, F. Xu, B. Wang and Y. Wei, *Nanomaterials*, 2021, **11**, 559.
- 67 V. Ivanovskaya, A. Zobelli, D. Teillet-Billy, N. Rougeau, V. Sidis and P. Briddon, *Eur. Phys. J. B*, 2010, **76**, 481–486.
- 68 A. Bafekry, M. Faraji, A. A. Ziabari, M. Fadlallah, C. V. Nguyen, M. Ghergherehchi and S. Fegghi, *New J. Chem.*, 2021, **45**, 8291–8296.
- 69 M. Born, K. Huang and M. Lax, *Am. J. Phys.*, 1955, **23**, 474.
- 70 Y. Guo, S. Zhou, Y. Bai and J. Zhao, *Appl. Phys. Lett.*, 2017, **110**, 163102.
- 71 R. C. Andrew, R. E. Mapasha, A. M. Ukpong and N. Chetty, *Phys. Rev. B: Condens. Matter Mater. Phys.*, 2012, **85**, 125428.
- 72 C. Shen, L. Wang, D. Wei, Y. Zhang, G. Qin, X.-Q. Chen and H. Zhang, arXiv preprint arXiv:2108.03671, 2021.
- 73 A. Bafekry, M. Faraji, D. M. Hoat, M. Shahrokhi, M. Fadlallah, F. Shojaei, S. Fegghi, M. Ghergherehchi and D. Gogova, *J. Phys. D: Appl. Phys.*, 2021, **54**, 155303.
- 74 E. L. Shirley, X. Zhu and S. G. Louie, *Phys. Rev. Lett.*, 1992, **69**, 2955.
- 75 J. Heyd, G. E. Scuseria and M. Ernzerhof, *J. Chem. Phys.*, 2003, **118**, 8207–8215.
- 76 J. Heyd, J. E. Peralta, G. E. Scuseria and R. L. Martin, *J. Chem. Phys.*, 2005, **123**, 174101.
- 77 J. Muscat, A. Wander and N. Harrison, *Chem. Phys. Lett.*, 2001, **342**, 397–401.
- 78 Q. Wu, L. Cao, Y. S. Ang and L. K. Ang, *Appl. Phys. Lett.*, 2021, **118**, 113102.
- 79 C.-c. Jian, X. Ma, J. Zhang and X. Yong, *J. Phys. Chem. C*, 2021, **125**, 15185–15193.
- 80 C. Peng, T. Zhou, P. Wei, W. Xu, H. Pan, F. Peng, J. Jia, K. Zhang and H. Yu, *APL Mater.*, 2021, **9**, 070703.
- 81 M. Jakhar, A. Kumar, P. K. Ahluwalia, K. Tankeshwar and R. Pandey, *Materials*, 2022, **15**, 2221.
- 82 Y. Wang, Z. Ding, N. Arif, W.-C. Jiang and Y.-J. Zeng, *Mater. Adv.*, 2022, **3**, 3389–3417.
- 83 M. Kwan, R. Winter, P. H. Mutin, M. Eizenberg and G. Ramanath, *Appl. Phys. Lett.*, 2017, **111**, 121602.
- 84 C. Nguyen, N. V. Hoang, H. V. Phuc, A. Y. Sin and C. V. Nguyen, *J. Phys. Chem. Lett.*, 2021, **12**, 5076–5084.
- 85 J. T. Robinson, J. Culbertson, M. Berg and T. Ohta, *Sci. Rep.*, 2018, **8**, 2006.
- 86 N. Bhalla, S. Taneja, P. Thakur, P. K. Sharma, D. Mariotti, C. Maddi, O. Ivanova, D. Petrov, A. Sukhachev, I. S. Edelman, et al., *Nano Lett.*, 2021, **21**, 9780–9788.
- 87 Z. Yu, W. Feng, W. Lu, B. Li, H. Yao, K. Zeng and J. Ouyang, *J. Mater. Chem. A*, 2019, **7**, 11160–11169.
- 88 A. Chaves, J. G. Azadani, H. Alsalman, D. Da Costa, R. Frisenda, A. Chaves, S. H. Song, Y. D. Kim, D. He, J. Zhou, et al., *npj 2D Mater. Appl.*, 2020, **4**, 29.
- 89 S. Yang, Y. Chen and C. Jiang, *InfoMat*, 2021, **3**, 397–420.
- 90 Y. Sun, S. Thompson and T. Nishida, *J. Appl. Phys.*, 2007, **101**, 104503.
- 91 J. Guo, Z. Zhou, H. Li, H. Wang and C. Liu, *Nanoscale Res. Lett.*, 2019, **14**, 174.
- 92 Y. Ma, X. Zhao, M. Niu, X. Dai, W. Li, Y. Li, M. Zhao, T. Wang and Y. Tang, *RSC Adv.*, 2017, **7**, 25582–25588.
- 93 F. Liu, J. Zhou, C. Zhu and Z. Liu, *Adv. Funct. Mater.*, 2017, **27**, 1602404.
- 94 F. Motazedian, J. Zhang, Z. Wu, D. Jiang, S. Sarkar, M. Martyniuk, C. Yan, Y. Liu and H. Yang, *Mater. Des.*, 2021, **197**, 109257.
- 95 S. Bruzzone and G. Fiori, *Appl. Phys. Lett.*, 2011, **99**, 222108.
- 96 B. Mortazavi, F. Shojaei, B. Javvaji, T. Rabczuk and X. Zhuang, *Mater. Today Energy*, 2021, **22**, 100839.

